

# Multiple Control of Few-layer Janus MoSSe Systems

Shuanglong Liu,<sup>1,2</sup> James N. Fry,<sup>1</sup> and Hai-Ping Cheng<sup>1,2,3\*</sup>

<sup>1</sup>*Department of Physics, University of Florida, Gainesville, Florida 32611, USA*

<sup>2</sup>*Quantum Theory Project, University of Florida, Gainesville, Florida 32611, USA*

<sup>3</sup>*Center for Molecular Magnetic Quantum Materials,  
University of Florida, Gainesville, Florida 32611, USA*

(Dated: January 26, 2022)

# Abstract

In this computational work based on density functional theory we study the electronic and electron transport properties of asymmetric multi-layer MoSSe junctions, known as Janus junctions. Focusing on 4-layer systems, we investigate the influence of electric field, electrostatic doping, strain, and interlayer stacking on the electronic structure. We discover that a metal to semiconductor transition can be induced by an out-of-plane electric field. The critical electric field for such a transition can be reduced by in-plane biaxial compressive strain. Due to an intrinsic electric field, a 4-layer MoSSe can rectify out-of-plane electric current. The rectifying ratio reaches 34.1 in a model junction Zr/4-layer MoSSe/Zr. This ratio can be further enhanced by increasing the number of MoSSe layers. In addition, we show a drastic sudden vertical compression of 4-layer MoSSe due to in-plane biaxial tensile strain, indicating a second phase transition. Furthermore, an odd-even effect on electron transmission at the Fermi energy for Zr/ $n$ -layer MoSSe/Zr junctions with  $n = 1, 2, 3, \dots, 10$  is observed. These findings reveal the richness of physics in this asymmetric system and strongly suggest that the properties of 4-layer MoSSe are highly tunable, thus providing a guide to future experiments relating materials research and nanoelectronics.

## I. INTRODUCTION

Two-dimensional (2D) transition metal dichalcogenides (TMDs) have potential applications in electronics/optoelectronics [1, 2], due to the presence of a direct band gap and sufficiently high mobility. The computed band gaps of TMDs vary by  $\sim 2$  eV, depending on the chemical composition [3], which provides rich opportunities for different applications. In 2017, a semiconducting Janus transition metal dichalcogenide MoSSe was synthesized in experiments independently by Zhang *et al.* [4] and by Lu *et al.* [5], where One face of MoSSe consists of S atoms and the other of Se atoms. Such a discovery has inspired a surge of research into Janus 2D materials, including but not limited to MoSSe [6–16]. For example, superior charge carrier mobility was predicted in monolayer WSSe [6, 7], and large piezoelectricity was reported in monolayer Te<sub>2</sub>Se [8] and monolayer MoSO [9]. Strong Dzyaloshinskii-Moriya interaction was found in Janus manganese dichalcogenides [10, 11] and Janus chromium trihalides [12, 13].

---

\* [hping@ufl.edu](mailto:hping@ufl.edu)

Since the electron affinity of S is lower than that of Se, there is electron accumulation on the S side of monolayer MoSSe. Consequently, monolayer MoSSe possesses an intrinsic out-of-plane electric dipole, pointing from S to Se. Multilayer MoSSe can have a potential buildup in the out-of-plane direction if the electric dipoles of individual layers are aligned in the same direction. In this case, the band gap of multilayer MoSSe decreases with the number of MoSSe layers  $n$ , until it closes at  $n = 4$  [17]. Since it is the intrinsic electric field that causes the band gap closing in 4-layer MoSSe, we wondered whether the band gap can reopen upon the application of a compensating external electric field. It is not a surprise, as we will show in the results section, that a metal to semiconductor transition in 4-layer MoSSe can be induced by an external out-of-plane electric field. However, the critical electric field that is required to induce the metal to semiconductor transition in 4-layer MoSSe is much smaller than that for a semiconductor to metal transition in bilayer MoS<sub>2</sub> [18]. In the context of a field effect transistor, an external electric field can be applied via a dual gate configuration, whereas a single gate configuration induces electrostatic doping. We will also show how the electronic structure of 4-layer MoSSe is affected by electrostatic doping. Furthermore, the internal electric field within 4-layer MoSSe may allow rectification of an out-of-plane electric current, which sets another research goal of this study.

Guo and Dong showed that the band gap of monolayer MoSSe can be significantly tuned by in-plane biaxial strain. [19] Strain engineering of the electronic structure of heterogeneous bilayers MoSSe/WX<sub>2</sub> (X=S, Se) [20] and MoSSe/WSSe [21] have also been reported. These discoveries motivate us to investigate the influence of in-plane biaxial strain on the critical electric field for the metal to semiconductor transition. In addition, we will also examine the influence of out-of-plane pressure on the critical electric field.

The rest of the paper is organized as follows. In Section II, we present the computational methods and simulation parameters. We then show our computational results in Section III, which is further divided into subsections concerning the atomic structure, external electric field, electrostatic doping, strain, and rectifying effect respectively. Finally, conclusions are given in Section IV.

## II. METHOD

Our calculations are based on density functional theory (DFT) [22, 23] as implemented in the SIESTA package [24]. The effective screening medium (ESM) method is used to simulate the effects of out-of-plane electric field and electrostatic doping [25, 26]. The DFT + NEGF method [27–29] is used to simulate electron transport properties of a Zr/4-layer MoSSe/Zr junction. We calculate the electron transmission and the electric current via the Caroli formula [30] and the Landauer formula [31, 32] respectively.

We apply a double- $\zeta$  polarized (DZP) basis set [24] to expand the Kohn-Sham orbitals and the electron density. A mesh cutoff of 150 Ry is set to sample real space. A  $15 \times 15$  Monkhorst-Pack  $k$ -point mesh [33] is chosen to sample the 2D reciprocal space for ionic relaxations. For self-consistent calculations, the  $k$ -point mesh is increased to  $21 \times 21$  to guarantee convergence. The  $k$ -point mesh is further increased to  $101 \times 101$  for calculating electron transmission. We adopt norm-conserving pseudo-potentials as generated by the Troullier-Martins scheme [34] and the Perdew-Burke-Ernzerhof (PBE) exchange correlation energy functional [35]. The Van der Waals interaction is taken into account via the DFT-D2 method [36]. The atomic structure of 4-layer MoSSe is fully optimized in all our calculations except for those under finite bias, since the atomic force under non-equilibrium conditions may not be reliable. The numerical tolerances for the density matrix, the Hamiltonian matrix, and the atomic force are no larger than  $1 \times 10^{-4}$ ,  $2 \times 10^{-3}$  eV, and  $0.02$  eV/Å respectively.

## III. RESULTS

We present our results in five parts. In Section III A, we first display our atomic structure of 4-layer MoSSe. Next, in Section III B we show a metal to semiconductor transition in 4-layer MoSSe induced by an out-of-plane external electric field. Third is Section III C, on the effects of electrostatic doping due to a single back gate. Fourth, we examine how the critical electric field for the metal to semiconductor transition is affected by in-plane biaxial strain in Section III D. Last, we demonstrate that 4-layer MoSSe can rectify out-of-plane electric current in Section III E.

## A. Atomic structure

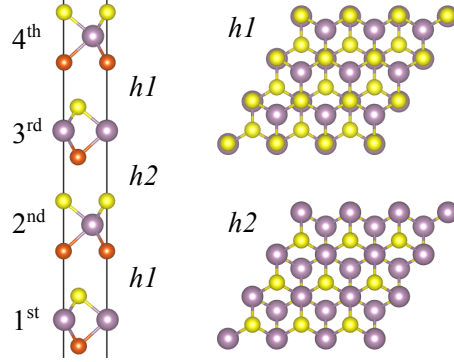


FIG. 1. Left: Side view of the 4-layer MoSSe under study. Label *h1* (*h2*) identifies a type 1 (type 2) hollow site interlayer stacking. Upper (lower) right: Top view of a bilayer MoSSe with *h1* (*h2*) interlayer stacking.

Our atomic structure of 4-layer MoSSe is shown on the left of Fig. 1. The S (Se) side of each MoSSe layer faces upward. Adjacent MoSSe layers adopt a hollow site interlayer stacking, which is energetically more favorable than on-top site interlayer stacking [37, 38]. There are two types of hollow site interlayer stacking, as shown on the right in Fig. 1. Type 1 hollow site interlayer stacking (*h1*) is slightly higher in energy than type 2 hollow site interlayer stacking (*h2*) [37, 38]. In this study, we focus on the 4-layer MoSSe with a stacking sequence of *h1-h2-h1*. Nevertheless, we also verify our major findings for *h1-h1-h1* stacking 4-layer MoSSe and *h2-h2-h2* stacking 4-layer MoSSe.

## B. Out-of-plane electric field

The inset of Fig. 2a illustrates our model setup for applying an out-of-plane electric field to 4-layer MoSSe. The 4-layer MoSSe is placed between two metal plates, a bottom gate and a top gate, separated by a distance  $L$ . The two gates have constant electrostatic potentials,  $V_{\text{BG}}$  ( $V_{\text{TG}}$ ) for the bottom (top) gate. Electric field in this work refers to the average electric field between the two gates,

$$E = (V_{\text{TG}} - V_{\text{BG}})/L. \quad (1)$$

Each gate is spaced from the Janus MoSSe by a distance  $d \sim 15 \text{ \AA}$  of vacuum. The four MoSSe layers from bottom to the top are labeled as 1<sup>st</sup>, 2<sup>nd</sup>, 3<sup>rd</sup>, and 4<sup>th</sup> layer respectively

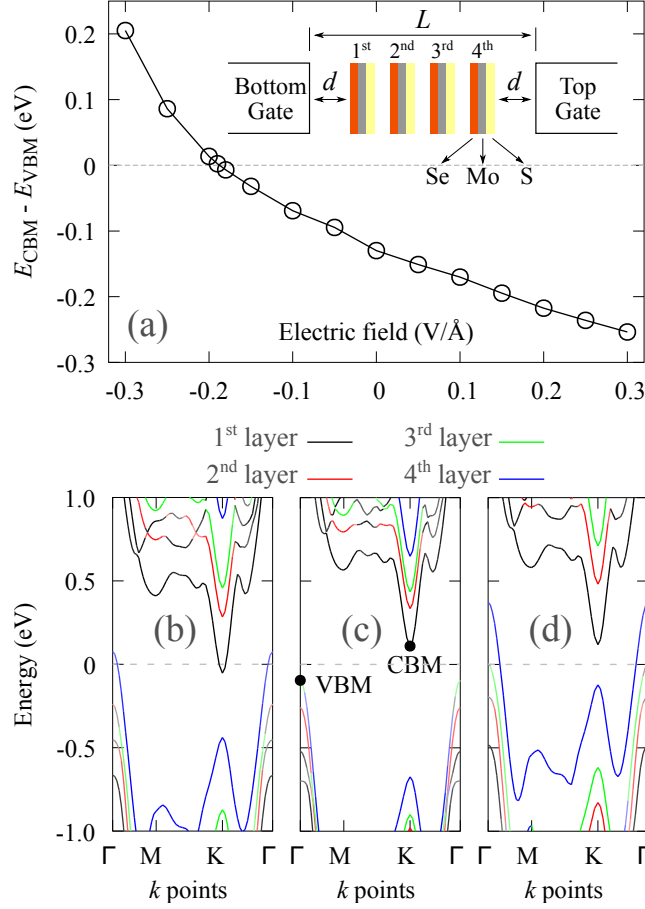


FIG. 2. (a) Energy difference between the conduction band minimum (CBM) and the valence band maximum (VBM) of the 4-layer MoSSe under different electric fields. The inset illustrates the system setup. (b)–(d) Band structures of the 4-layer MoSSe under zero,  $-0.30$ , and  $+0.30$  V/Å electric fields respectively. Colors identify the layer from which the band mainly originates (see text). The CBM and the VBM are marked in panel (c).

. The sulfur side faces the top gate.

Fig. 2b shows the band structure of the 4-layer MoSSe under zero electric field. Roughly speaking, an energy band is colored black (red, green, blue) if it originates mainly from the 1<sup>st</sup> (2<sup>nd</sup>, 3<sup>rd</sup>, 4<sup>th</sup>) layer. The details of colormap are given in Appendix A. We see from Fig. 2b that the 4-layer MoSSe is metallic with the 1<sup>st</sup> (4<sup>th</sup>) layer being electron- (hole-) doped. If a negative electric field of  $-0.30$  V/Å is applied, an energy gap of 0.20 eV opens up around the Fermi energy, and the 4-layer MoSSe becomes a semiconductor (Fig. 2c). In contrast, the 4-layer MoSSe remains a metal if a positive electric field of  $+0.30$  V/Å is

applied (Fig. 2d). In order to find the critical electric field for the metal to semiconductor transition, we examine the energy difference between the conduction band minimum (CBM) and the valence band maximum (VBM) versus electric field in Fig. 2a. The energy difference  $E_{\text{CBM}} - E_{\text{VBM}}$  decreases with electric field, and it reaches zero at a critical electric field of  $\sim -0.187 \text{ V/\AA}$ .

These results are for the 4-layer MoSSe with  $h1$ - $h2$ - $h1$  stacking. The critical electric field for the  $h1$ - $h1$ - $h1$  and  $h2$ - $h2$ - $h2$  stackings are  $-0.252 \text{ V/\AA}$  and  $-0.145 \text{ V/\AA}$ , respectively. Compared with the  $h1$ - $h2$ - $h1$  stacking, the  $h1$ - $h1$ - $h1$  ( $h2$ - $h2$ - $h2$ ) stacking has a larger (smaller) critical field in magnitude. In order to understand such a difference, we analyse the internal potential buildup between adjacent MoSSe layers. In practice, we take the planar average of the electrostatic potential over the 2D plane parallel to the Janus MoSSe. Denoting the plane averaged electrostatic potential at the vertical position of a Se/S atom as  $V_{\text{Se/S}}$ , we find that the potential buildup  $V_{\text{Se}} - V_{\text{S}}$  at the three van der Waals gaps of the 4-layer MoSSe with  $h1$ - $h2$ - $h1$  stacking are 1.39 eV ( $h1$ ), 1.22 eV ( $h2$ ), and 1.44 eV ( $h1$ ) respectively. As such, the potential buildup at a van der Waals gap between two MoSSe layers with  $h1$  stacking is larger than that for  $h2$  stacking by 0.17/0.22 eV. A larger internal electric field requires a larger external electric field to compensate and to open a band gap around the Fermi level. Therefore, the critical electric field for the  $h1$ - $h1$ - $h1$  ( $h2$ - $h2$ - $h2$ ) stacking is larger (smaller) than that for the  $h1$ - $h2$ - $h1$  stacking.

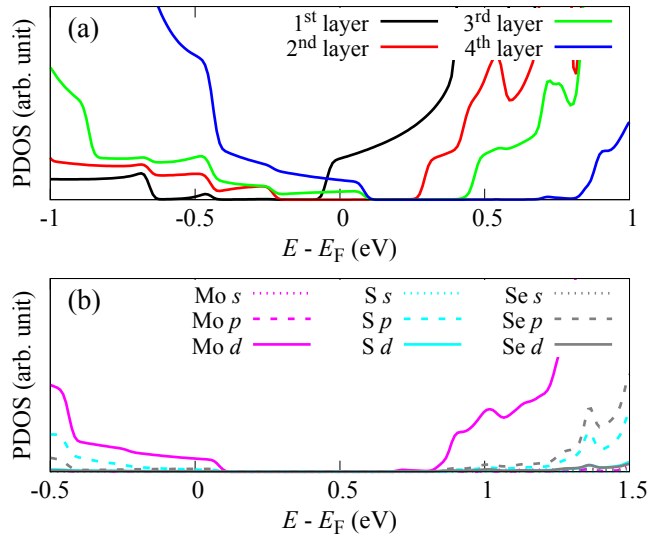


FIG. 3. Projected density of states (PDOS) of (a) each MoSSe layer, and (b) the  $s$ -,  $p$ -, and  $d$ -orbitals in the 1<sup>st</sup> MoSSe layer. The Fermi energy is set to zero.

Fig. 3a shows the layer-decomposed projected density of states (PDOS) for 4-layer MoSSe with *h1-h2-h1* stacking under zero external electric field. Recall that 4-layer MoSSe is metallic in such a way that both the valence and the conduction bands cross the Fermi energy. As seen from Fig. 3a, the conduction-band states around the Fermi level originate merely from the 1<sup>st</sup> MoSSe layer while the valence-band states around the Fermi level originate from both the 3<sup>rd</sup> and the 4<sup>th</sup> MoSSe layers. Furthermore, the PDOS of the 4<sup>th</sup> MoSSe layer is more than two times larger than the PDOS of the 3<sup>rd</sup> MoSSe layer at the Fermi level. There are not any states originating from the 2<sup>nd</sup> MoSSe layer at the Fermi level. Fig. 3b shows the orbital-decomposed PDOS for the 4<sup>th</sup> MoSSe layer. The states around both the VBM and the CBM are dominated by Mo *d* orbitals. The contribution from S or Se *p* orbitals to the valence (conduction) band becomes larger at lower (higher) energies. The contributions from all other orbitals are small within the energy range of  $[-0.5 : 1.5]$  eV. An analysis of the orbital-decomposed PDOS for the 3<sup>rd</sup> MoSSe layer (not shown in the figure) shows that there is a significant contribution of the S *p* orbitals to the states at the Fermi level. This indicates a hybridization between the 3<sup>rd</sup> and the 4<sup>th</sup> MoSSe layers.

### C. Electrostatic doping

In the previous section, we have shown that a metal to semiconductor transition can be induced by an out-of-plane electric field when the system is charge neutral. In this section, we examine the effects of electrostatic doping (charging) due to a back gate.

Fig. 4a shows the energy difference between the CBM and the VBM versus doping level for the 4-layer MoSSe with *h1-h2-h1* stacking subject to a single back gate. An energy gap between the CBM and the VBM can be induced by electron (hole) doping if the S (Se) side of 4-layer MoSSe faces the back gate. The gap-inducing external electric field for both Gate/[S-Mo-Se]<sub>4</sub> (the S side faces the back gate) and Gate/[Se-Mo-S]<sub>4</sub> (the Se side faces the back gate) is from the S side to the Se side of the 4-layer MoSSe, in accordance with the results in the previous section. Fig. 4b (Fig. 4c) shows the band structure of Gate/[S-Mo-Se]<sub>4</sub> (Gate/[Se-Mo-S]<sub>4</sub>) with a doping level such that an energy gap between the CBM and the VBM occurs. As seen from the figures, the Fermi level still crosses the conduction (valence) band. Therefore, electrostatic doping due to a single back gate does not induce metal to semiconductor transition.

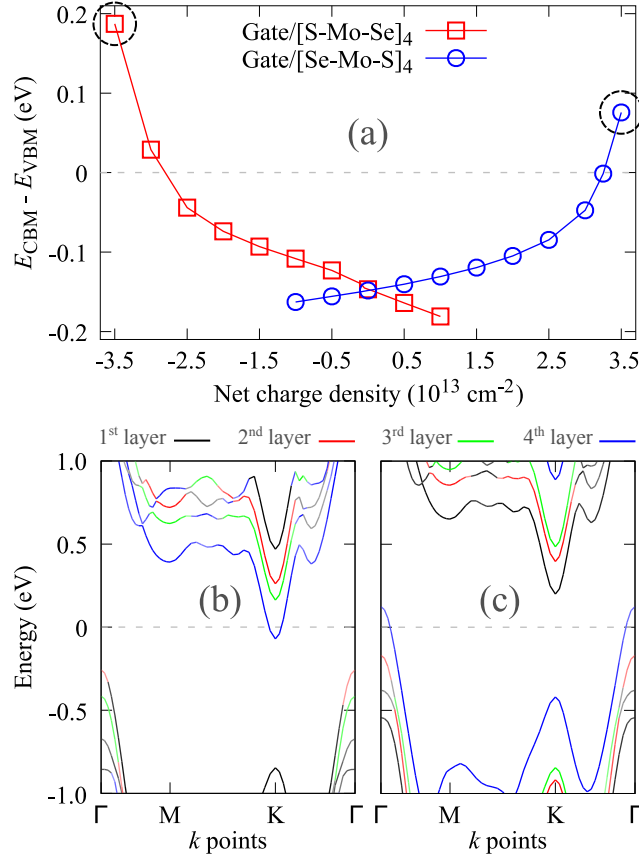


FIG. 4. (a) Energy difference between conduction band minimum (CBM) and valence band maximum (VBM). For red squares (blue circles) the S (Se) side of 4-layer MoSSe faces the back gate. (b) [(c)] Energy bands of Gate/[S-Mo-Se]<sub>4</sub> [Gate/[Se-Mo-S]<sub>4</sub>] under a doping level of  $-3.5$  [ $+3.5$ ]  $\times 10^{13} \text{ cm}^{-2}$  as indicated by the dashed circles in panel (a). Counting from the back gate, the four MoSSe layers are referred to as the 1<sup>st</sup>, 2<sup>nd</sup>, 3<sup>rd</sup>, and 4<sup>th</sup> layer respectively.

Figs. 4b and 4c also show that only the 4<sup>th</sup> MoSSe layer is conducting at low temperatures after an energy gap opens. Note that the 4<sup>th</sup> MoSSe layer is farthest away from the back gate. This phenomenon may be useful for electronic devices in which delicate control of conducting channels is required.

#### D. In-plane biaxial strain

The critical electric field of  $-0.187 \text{ V/\AA}$  is gigantic. In this section, we examine whether the critical field for the metal to semiconductor transition can be reduced by in-plane biaxial

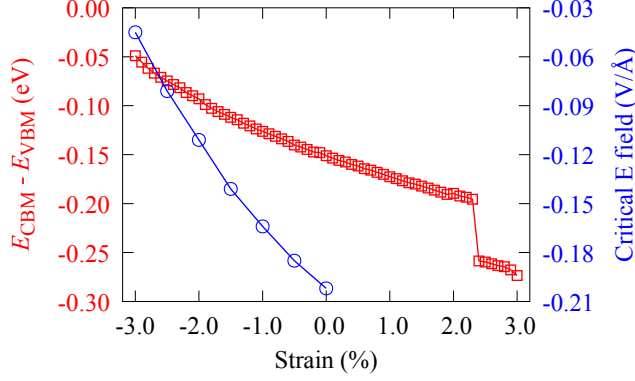


FIG. 5. Red squares show the energy difference between the conduction band minimum (CBM) and the valence band maximum (VBM) for 4-layer MoSSe as a function of in-plane biaxial strain (left-hand scale) Blue circles show the critical electric field for metal to semiconductor transition versus strain (right-hand scale).

strain.

The red squares in Fig. 5 shows the energy difference  $E_{\text{CBM}} - E_{\text{VBM}}$  versus strain. The strain is measured by  $(a - a_0)/a_0$ , where  $a$  is the lattice constant under a finite strain and  $a_0$  is the lattice constant under zero strain. A positive (negative) strain indicates tension (compression).  $E_{\text{CBM}} - E_{\text{VBM}}$ , which is always negative here, decreases (increases) with tensile (compressive) strain. Intuitively, a smaller  $|E_{\text{CBM}} - E_{\text{VBM}}|$  would require a smaller electric field to open an energy gap between the CBM and the VBM. Therefore, we search for the critical electric field at several compressive strains, and show the results as the blue circles in Fig. 5. Indeed, the magnitude of the critical field decreases with compressive strain. Under a compressive strain of  $-3.0\%$ , the magnitude of the critical field is reduced to  $-0.045 \text{ V/\AA}$ , which is more feasible in experiments.

For the 4-layer MoSSe with  $h1-h1-h1$  stacking under a compressive strain of  $-3.0\%$ ,  $E_{\text{CBM}} - E_{\text{VBM}}$  becomes  $-0.062 \text{ eV}$ . The corresponding critical electric field is  $-0.112 \text{ V/\AA}$  which is also significantly smaller in magnitude than the zero-strain value (of  $-0.252 \text{ V/\AA}$ ) for the same stacking.  $E_{\text{CBM}} - E_{\text{VBM}}$  is approximately  $0.007 \text{ eV}$  for the 4-layer MoSSe with  $h2-h2-h2$  stacking under a compressive strain of  $-3.0\%$ . A metal to semiconductor transition can be induced by a moderate compressive strain alone for the  $h2-h2-h2$  stacking. The critical in-plane biaxial strain is about  $-2.9\%$ .

At a strain of  $\sim 2.3\%$ , the energy difference  $E_{\text{CBM}} - E_{\text{VBM}}$  exhibits a sudden decrease.

This is accompanied with a sharp change in the thickness of the 4-layer MoSSe, by about 0.47 Å. More structural details concerning this sharp change are given in Appendix B. It is worth mentioning that the function of energy versus strain is smooth even at the strain of  $\sim 2.3\%$ .

We additionally simulate out-of-plane pressure by reducing the thickness of the 4-layer MoSSe with  $h1-h2-h1$  stacking. All atoms are relaxed except the bottom-most atomic layer and the top-most atomic layer. Our simulations show that  $E_{\text{CBM}} - E_{\text{VBM}}$  decreases (becoming more negative) as the thickness is reduced. For example, a reduction in the thickness by 0.5 Å leads to a decreases in  $E_{\text{CBM}} - E_{\text{VBM}}$  by about 0.06 eV. Thus, the critical electric field for metal to semiconductor transition is likely to increase with out-of-plane pressure.

### E. Rectifying effect

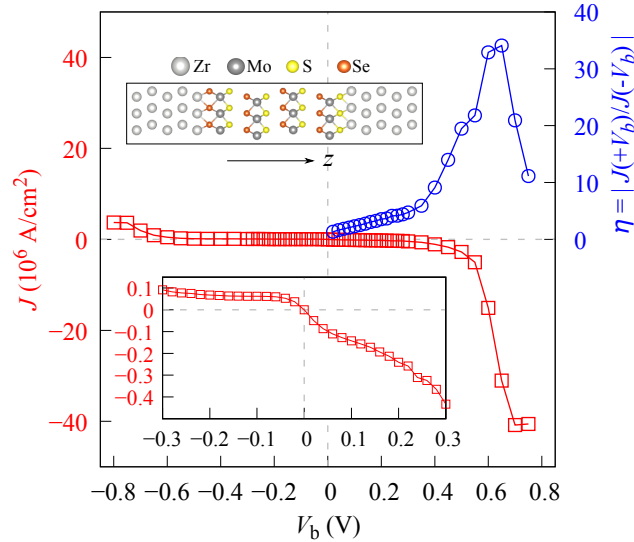


FIG. 6. Red squares show the electric current density in a Zr/4-layer MoSSe/Zr junction as a function of bias voltage. Blue circles show the rectifying ratio of the junction versus bias voltage. The inset zooms in on the central part of the junction.

Since 4-layer MoSSe has a substantial internal electric field, it may rectify out-of-plane electric current when employed in a circuit. Here, we present a proof-of-concept calculation where the 4-layer MoSSe with  $h1-h2-h1$  stacking is sandwiched between two zirconium electrodes, as shown in the upper inset of Fig. 6. A Zr electrode is chosen due to a small

lattice mismatch with MoSSe. The Zr/4-layer MoSS/Zr junction is periodic in the  $x$ - and  $y$ -directions, and electron transport is along the  $z$ -direction. Although only two finite pieces of Zr are shown in the inset, the left and right electrodes extend to infinity.

The red squares in Fig. 6 show the calculated electric current density  $J$  in the Zr/4-layer MoSS/Zr junction as a function of bias voltage. The bias voltage  $V_b$  is defined by

$$V_b = \mu_L - \mu_R, \quad (2)$$

where  $\mu_L$  ( $\mu_R$ ) is the chemical potential of the left (right) electrode. The  $J$ - $V_b$  curve at low bias voltages is zoomed in and shown in the lower inset.  $J(-0.02 \text{ V})$  is about  $3.7 \times 10^4 \text{ A/cm}^2$  which is on the same order with  $J(+0.02 \text{ V}) \sim -5.0 \times 10^4 \text{ A/cm}^2$ . Defining a rectifying ratio  $\eta$  as

$$\eta = |J(+V_b)/J(-V_b)|, \quad (3)$$

we see that  $\eta(0.02 \text{ V})$  is as small as 1.4. As shown by the blue circles in Fig. 6,  $\eta$  first gradually increases with bias voltage, reaching 4.7 at 0.3 V. As the bias voltage further increases in the positive direction, a sharp increase in the electric current density occurs at around 0.6 V. Such a sharp increase is however absent at negative bias voltages. As a result, a rectifying ratio as high as 34.1 is achieved at 0.65 V.  $\eta$  begins to decrease after 0.65 V, and is reduced to 11.1 at 0.75 V.

We next examine whether the rectifying ratio can be enhanced by tuning the number of MoSSe layers. Fig. 7 shows electron transmission as a function of energy  $T_n(E)$  for Zr/ $n$ -layer MoSSe/Zr junctions under zero bias with  $n = 1, 2, 3, \dots, 10$ . Setting the Fermi energy to zero, we observe that  $T_n(E)$  decays exponentially with  $n$  for  $E \in [-0.8 : 0] \text{ eV}$ . Particularly,  $T_{10}(E)$  is more than 10 orders of magnitude smaller than  $T_1(E)$  within this energy range. In contrast,  $T_n(E)$  is always above  $10^{-2}$  (and smaller than 1) regardless of  $n$  for  $E \in [0.5 : 0.8] \text{ eV}$ . Thus, we infer from the zero bias transmission function that thicker MoSSe should exhibit a higher rectifying ratio. We verify this idea using a Zr/5-layer MoSSe/Zr junction and obtain the higher value  $\eta = 85.6$  at  $V_b = 5.5 \text{ V}$ .

The electron transmission at Fermi energy decays differently with the number of MoSSe layers  $n$  depending on the parity of  $n$ . This odd-even effect originates from the parity-dependent potential buildup at the contact between the  $n$ -layer MoSSe and the right Zr electrode. Further analysis of this phenomenon is presented in Appendix C.

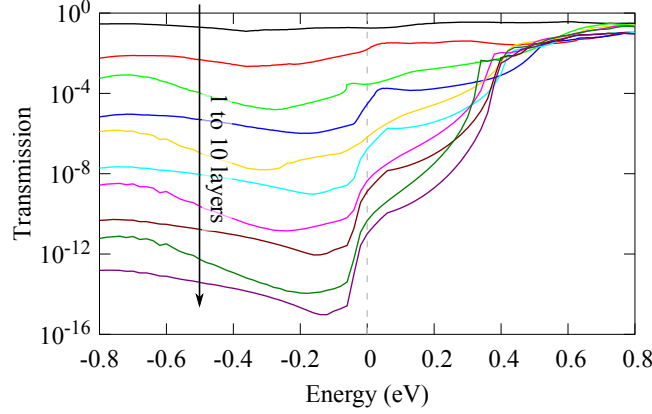


FIG. 7. Electron transmission versus energy for Zr/ $n$ -layer MoSSe/Zr junctions with  $n = 1, 2, 3, \dots, 10$ . The Fermi energy is set to zero.

#### IV. CONCLUSION

We have performed a detailed study of the electronic and electron transport properties of  $n$ -layer MoSSe ( $n = 1 - 10$ ) with focus on  $n = 4$  using first principles based density functional theory. Several significant findings obtained are as follows: 1) We show that a metal to semiconductor transition can be induced by an out-of-plane electric field; 2) Sensitive to the stacking order, the critical electric fields for the 4-layer MoSSe with  $h1$ - $h1$ - $h1$ ,  $h1$ - $h2$ - $h1$ , and  $h2$ - $h2$ - $h2$  stackings are, respectively,  $-0.252$ ,  $-0.187$ , and  $-0.145$  V/Å; 3) The critical electric field for the  $h1$ - $h1$ - $h1$  stacking is highest (in magnitude) because the internal potential buildup with a  $h1$  stacking is larger than that with a  $h1$  stacking. We can reduce the critical electric field by applying a in-plane biaxial compressive strain, and this works for all the three stackings; 4) The applied strain induces a second phase transition indicated by a sudden compression in the vertical dimension; 5) The 4-layer MoSSe with  $h1$ - $h2$ - $h1$  stacking is always metallic upon electrostatic doping, although an energy gap between the conduction minimum and the valence maximum can be opened; 6) When sandwiched between two Zr electrodes, the 4-layer MoSSe can rectify electric current with a maximum rectifying ratio of 34.1 at 0.65 V; and 7) finally, the rectifying ratio can be enhanced by increasing the number of MoSSe layers. Concluded from a high-level computational approach, these results have predicting power. One can use a combination of these controlling parameters to guide future experiments in areas of material design and nanoelectronics.

## ACKNOWLEDGMENTS

This work is supported by the US Department of Energy (DOE), Office of Basic Energy Sciences (BES), under Contract No. DE-FG02-02ER45995. Computations were done using the utilities of the National Energy Research Scientific Computing Center and University of Florida Research Computing.

## Appendix A: Colormap for Fig. 2

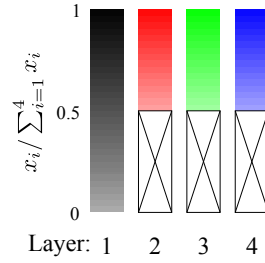


FIG. A1. Colormap of the relative projected density of states (PDOS) from each MoS<sub>2</sub> layer.  $x_i$  represents the PDOS from the  $i$ th layer.

Fig. A1 shows the colormap for Fig. 2 in the main text. It is generated using the following script for Gnuplot.

```
set palette model RGB
set palette color
set palette defined ( \
0.0 "#aaaaaa", 0.2 "#808080", 1.0 "#000000", \
1.1 "#ffffff", 1.2 "#ffffff", 2.0 "#ff0000", \
2.1 "#ffffff", 2.2 "#ffffff", 3.0 "#00ff00", \
3.1 "#ffffff", 3.2 "#ffffff", 4.0 "#0000ff" )
```

```
g(x1, x2, x3, x4) = \
x1 / (x1 + x2 + x3 + x4) > 0.5 ? x1 / (x1 + x2 + x3 + x4) : \
x2 / (x1 + x2 + x3 + x4) > 0.5 ? x2 / (x1 + x2 + x3 + x4) + 1 : \
x3 / (x1 + x2 + x3 + x4) > 0.5 ? x3 / (x1 + x2 + x3 + x4) + 2 : \
```

$$x_4/(x_1+x_2+x_3+x_4) > 0.5 \quad ? \quad x_4/(x_1+x_2+x_3+x_4) + 3 : \backslash$$

$$x_1/(x_1+x_2+x_3+x_4)$$

p "bands.dat" u 1:2:(g(\$3,\$4,\$5,\$6)) w l palette

In this script,  $x_i$  is the projected density of states (PDOS) of the  $i$ th MoSSe layer due to a Kohn-Sham state. If the ratio  $\tau_i = x_i/(x_1 + x_2 + x_3 + x_4)$  is greater than 0.5, then the contribution from the  $i$ th layer dominates. We identify the dominant layer index by color type (black, red, green, or blue), and represent the value of  $\tau_i$  by color brightness. If none of  $\tau_i$  ( $i = 1, 2, 3, 4$ ) is greater than 0.5, then we use a grayscale according to the value of  $\tau_1$ .

## Appendix B: Abrupt structural change

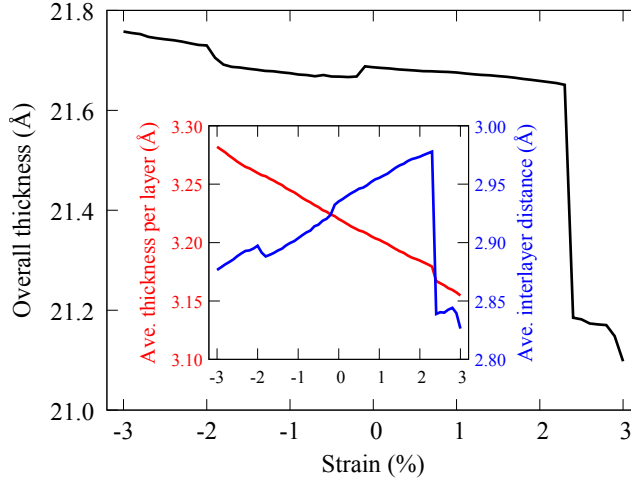


FIG. B1. Thickness of 4-layer MoSSe versus in-plane biaxial strain. Inset: Average thickness per MoSSe layer and average interlayer distance versus in-plane biaxial strain.

Fig. B1 shows the overall thickness of 4-layer MoSSe with  $h1-h2-h1$  stacking versus in-plane biaxial strain. The thickness gradually decreases with tensile strain before a sharp decrease of  $0.47 \text{ \AA}$  occurs at a strain of 2.3%. This sharp decrease is due to both an abrupt decrease in the thickness of an individual MoSSe layer and an abrupt decrease in the interlayer distance (see the inset of Fig. B1). As the strain increases from 2.3% to 2.4%, the change in the average interlayer distance is  $0.139 \text{ \AA}$ , which is about 11 times larger than the change in the average thickness of individual MoSSe layers. Thus the sharp decrease in the

overall thickness is dominated by the decrease in the interlayer distance. Differently, the gradual decrease in the overall thickness at small tensile strain is dominated by the decrease in the thickness of individual MoSSe layers.

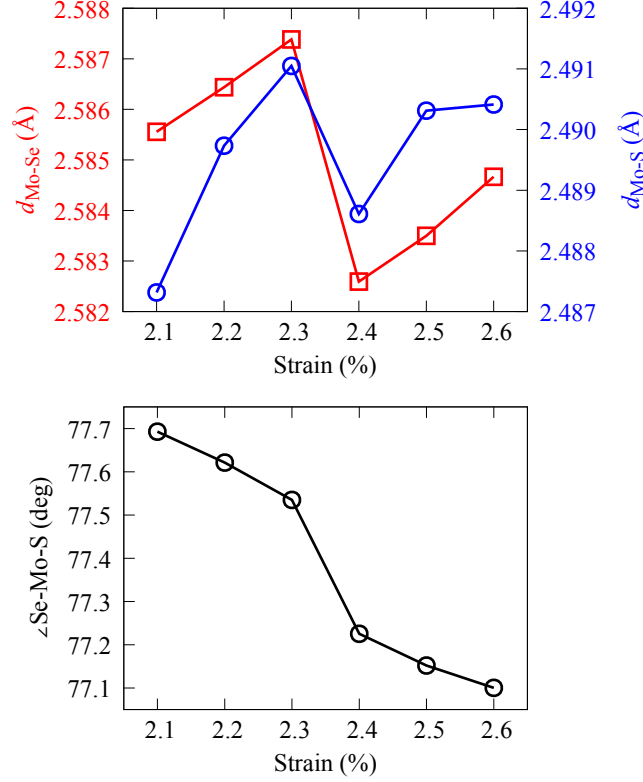


FIG. B2. Bond lengths (upper panel) and bond angle (lower panel) of the 4<sup>th</sup> MoSSe layer of 4-layer MoSSe near the critical strain.

In order to reveal the changes in bond length and bond angle within a MoSSe monolayer, we choose the 4<sup>th</sup> MoSSe layer as a representative. As shown in the upper panel of Fig. B2, both the Mo–Se and Mo–S bond lengths  $d_{\text{Mo-Se}}$  and  $d_{\text{Mo-S}}$  increase with strain before (strain < 2.3%) and after (strain > 2.4%) the sharp decrease in the overall thickness of the 4-layer MoSSe. However,  $d_{\text{Mo-Se}}$  ( $d_{\text{Mo-S}}$ ) decreases by about 0.005 Å (0.003 Å) as the strain increases from 2.3% to 2.4%. The lower panel of Fig. B2 shows the bond angle  $\angle \text{Se-Mo-S}$  versus the strain. The angle always decreases with strain, but the decrease is slightly faster for  $2.3\% \leq \text{strain} \leq 2.4\%$ . The reduction of the Mo–Se and Mo–S bond lengths together with a faster decrease in the bond angle  $\angle \text{Se-Mo-S}$  signify the sharp decrease of the thickness of a MoSSe monolayer.

## Appendix C: Odd-even effect

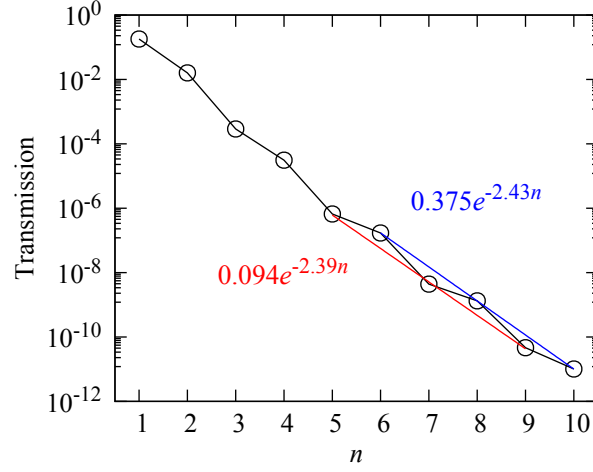


FIG. C1. Electron transmission at the Fermi energy for Zr/ $n$ -layer MoSSe/Zr junctions versus the number of layers  $n$ .

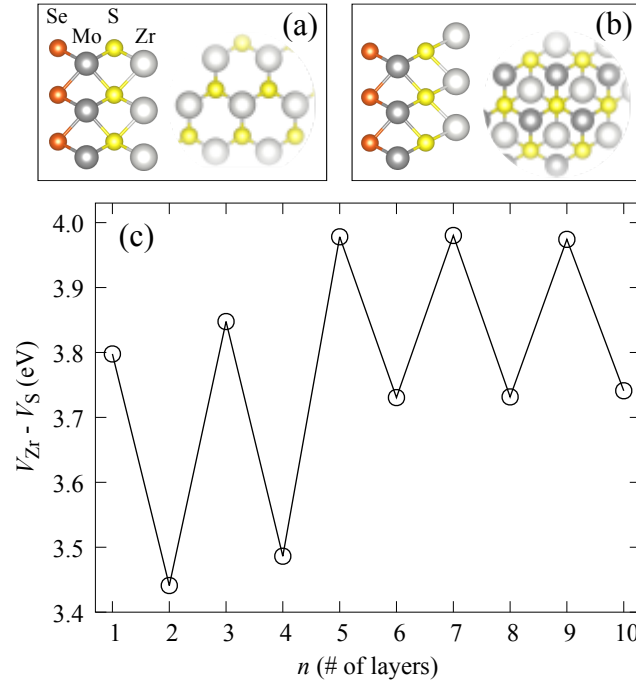


FIG. C2. (a) [(b)] Top and side views of the contact between MoSSe and Zr on the right side of Zr/ $n$ -layer MoSSe/Zr junctions with  $n$  being odd [even]. (c) Difference between the plane averaged electrostatic potential at Zr and that at S at the contact shown in panels (a) and (b).

Fig. C1 shows the electron transmission at the Fermi energy  $T_n(E_F)$  for Zr/ $n$ -layer

MoSSe/Zr junctions under zero bias with  $n = 1, 2, 3, \dots, 10$ . For simplicity, we will write  $T_n(E_F)$  as  $T_n$  in the rest of this section. As seen from the figure,  $T_n$  decays differently for even  $n$  and odd  $n$ . When  $n \geq 5$ ,  $T_n$  can be well fit by a function of the form  $T_n = \lambda e^{-\gamma n}$ ,  $T_n^o \approx 9.44 \times 10^{-2} e^{-2.39}$  for odd  $n$  and  $T_n^e \approx 3.75 \times 10^{-1} e^{-2.43n}$  for even  $n$ . The fitted curves are also shown in Fig. C1. Interpolating, we see that  $T_n^o < T_n^e$  at the same number of layers  $n$ , or the same width of an effective tunneling barrier. As such, we infer that the height of the effective tunneling barrier in odd junctions is higher than in even junctions.

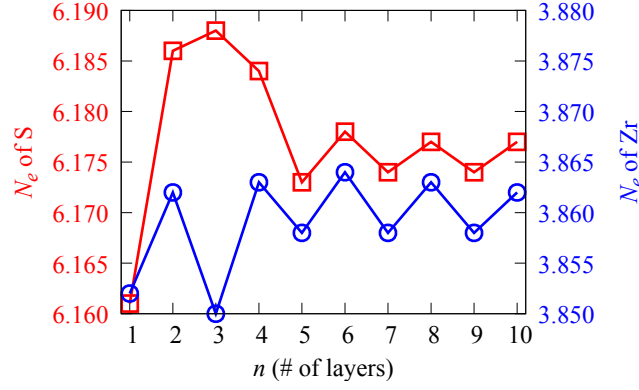


FIG. C3. Mulliken charge analysis: the number of electrons per S or Zr atom at the right contact of Zr/ $n$ -layer MoSSe/Zr junctions versus the number of MoSSe layers  $n$ .

There are two possible reasons for such a difference in the height of the tunneling barrier. The first one lies in the  $n$ -layer MoSSe itself. Recall that the potential buildup at each van der Waals gap is stacking-dependent and that the potential buildup at an  $h1$  stacking is larger. Given that the number of  $h1$  stackings is greater (lesser) than the number of  $h2$  stackings by one in even (odd) junctions, we expect that even junctions have a higher effective barrier. However, this is contradictory to the fact that  $T_n^o < T_n^e$ . The second possible reason pertains to the contact between the  $n$ -layer MoSSe and the Zr electrodes. The contact between the left Zr electrode and the  $n$ -layer MoSSe is the same for all the junctions, while the contact on the right side is different for even and odd junctions, as depicted in Figs. C2a and C2b. As a consequence, there is a parity-dependent potential difference between the adjacent Zr and S atomic layers as shown in Fig. C2c. For  $n \geq 5$ , the odd junctions possess an  $\sim 0.25$  eV higher potential difference  $V_{Zr} - V_S$  than the even junctions. It seems that the potential buildup at the right contact competes with the potential buildup at van der Waals gaps within a multilayer MoSSe, with the former being dominant. Therefore, the

effective tunneling barrier of odd junctions is higher than that of even junctions. It is worth mentioning that the number of electrons at the right contact also exhibits an oscillatory behavior for  $n \geq 5$ , as shown in Fig. C3.

- 
- [1] B. Radisavljevic, A. Radenovic, J. Brivio, V. Giacometti, and A. Kis, [Nature Nanotechnology](#) **6**, 147 (2011).
  - [2] D. Lembke, S. Bertolazzi, and A. Kis, [Accounts of Chemical Research](#) **48**, 100 (2015).
  - [3] F. A. Rasmussen and K. S. Thygesen, [Journal of Physical Chemistry C](#) **119**, 13169 (2015).
  - [4] J. Zhang, S. Jia, I. Kholmanov, L. Dong, D. Q. Er, W. B. Chen, H. Guo, Z. H. Jin, V. B. Shenoy, L. Shi, and J. Lou, [Acs Nano](#) **11**, 8192 (2017).
  - [5] A. Y. Lu, H. Y. Zhu, J. Xiao, C. P. Chuu, Y. M. Han, M. H. Chiu, C. C. Cheng, C. W. Yang, K. H. Wei, Y. M. Yang, Y. Wang, D. Sokaras, D. Nordlund, P. D. Yang, D. A. Muller, M. Y. Chou, X. Zhang, and L. J. Li, [Nature Nanotechnology](#) **12**, 744 (2017).
  - [6] J. Wang, H. B. Shu, T. F. Zhao, P. Liang, N. Wang, D. Cao, and X. S. Chen, [Physical Chemistry Chemical Physics](#) **20**, 18571 (2018).
  - [7] C. X. Xia, W. Q. Xiong, J. Du, T. X. Wang, Y. T. Peng, and J. B. Li, [Physical Review B](#) **98**, 165424 (2018).
  - [8] Y. Chen, J. Y. Liu, J. B. Yu, Y. G. Guo, and Q. Sun, [Physical Chemistry Chemical Physics](#) **21**, 1207 (2019).
  - [9] M. Yagmurcukardes and F. M. Peeters, [Physical Review B](#) **101**, 155205 (2020).
  - [10] J. R. Yuan, Y. M. Yang, Y. Q. Cai, Y. H. Wu, Y. P. Chen, X. H. Yan, and L. Shen, [Physical Review B](#) **101**, 094420 (2020).
  - [11] J. H. Liang, W. W. Wang, H. F. Du, A. L. Hall, K. R. Garcia, M. R. E. Chshiev, A. E. Fert, and H. X. Yang, [Physical Review B](#) **101**, 184401 (2020).
  - [12] C. S. Xu, J. S. Feng, S. Prokhorenko, Y. Nahas, H. J. Xiang, and L. Bellaiche, [Physical Review B](#) **101**, 060404(R) (2020).
  - [13] F. Zhang, H. Zhang, W. B. Mi, and X. C. Wang, [Physical Chemistry Chemical Physics](#) **22**, 8647 (2020).
  - [14] C. M. Zhang, Y. H. Nie, S. Sanvito, and A. J. Du, [Nano Letters](#) **19**, 1366 (2019).
  - [15] H. R. Jappor, M. M. Obeid, T. V. Vu, D. M. Hoat, H. D. Bui, N. N. Hieu, S. J. Edrees,

- Y. Mogulkoc, and R. Khenata, [Superlattices and Microstructures](#) **130**, 545 (2019).
- [16] F. Zhang, W. B. Mi, and X. C. Wang, [Advanced Electronic Materials](#) **6**, 1900778 (2020).
- [17] A. C. Riis-Jensen, M. Pandey, and K. S. Thygesen, [Journal of Physical Chemistry C](#) **122**, 24520 (2018).
- [18] Q. H. Liu, L. Z. Li, Y. F. Li, Z. X. Gao, Z. F. Chen, and J. Lu, [Journal of Physical Chemistry C](#) **116**, 21556 (2012).
- [19] S. D. Guo and J. Dong, [Semiconductor Science and Technology](#) **33**, 085003 (2018).
- [20] C. Yu and Z. G. Wang, [Physica Status Solidi B-Basic Solid State Physics](#) **256**, 1900261 (2019).
- [21] W. Y. Guo, X. Ge, S. T. Sun, Y. Q. Xie, and X. Ye, [Physical Chemistry Chemical Physics](#) **22**, 4946 (2020).
- [22] P. Hohenberg and W. Kohn, [Physical Review B](#) **136**, B864 (1964).
- [23] W. Kohn and L. J. Sham, [Physical Review](#) **140**, 1133 (1965).
- [24] J. M. Soler, E. Artacho, J. D. Gale, A. Garcia, J. Junquera, P. Ordejon, and D. Sanchez-Portal, [Journal of Physics-Condensed Matter](#) **14**, 2745 (2002).
- [25] M. Otani and O. Sugino, [Physical Review B](#) **73**, 115407 (2006).
- [26] H.-P. Cheng, S. Liu, X. Chen, L. Zhang, and J. N. Fry, [AVS Quantum Science](#) **2**, 027101 (2020).
- [27] J. Taylor, H. Guo, and J. Wang, [Physical Review B](#) **63**, 121104(R) (2001).
- [28] Y. Q. Xue, S. Datta, and M. A. Ratner, [Chemical Physics](#) **281**, 151 (2002).
- [29] M. Brandbyge, J. L. Mozos, P. Ordejon, J. Taylor, and K. Stokbro, [Physical Review B](#) **65**, 165401 (2002).
- [30] C. Caroli, R. Combescot, P. Nozieres, and D. Saint-James, [Journal of Physics C: Solid State Physics](#) **4**, 916 (1971).
- [31] R. Landauer, [Ibm Journal of Research and Development](#) **1**, 223 (1957).
- [32] R. Landauer, [Philosophical Magazine](#) **21**, 863 (1970).
- [33] H. J. Monkhorst and J. D. Pack, [Physical Review B](#) **13**, 5188 (1976).
- [34] N. Troullier and J. L. Martins, [Physical Review B](#) **43**, 1993 (1991).
- [35] J. P. Perdew, K. Burke, and M. Ernzerhof, [Physical Review Letters](#) **77**, 3865 (1996).
- [36] S. Grimme, [Journal of Computational Chemistry](#) **27**, 1787 (2006).
- [37] W. J. Yin, B. Wen, G. Z. Nie, X. L. Wei, and L. M. Liu, [Journal of Materials Chemistry C](#) **6**, 1693 (2018).

[38] Z. Y. Guan, S. Ni, and S. L. Hu, [Journal of Physical Chemistry C](#) **122**, 6209 (2018).